Title

Characterization of a collimated neutron imager for low-rate fast neutron imaging

Authors
Glick, Adam
Brubaker, Erik
Cabrera-Palmer, Belkis
et al.

Publication Date
2022-03-01

DOI
10.1016/j.nima.2021.166230

Characterization of a collimated neutron imager for low-rate fast neutron imaging

Adam Glick[a], Erik Brubaker[b], Belkis Cabrera-Palmer[b], Mark Gerling[b], Ethan S. Boado[a], Kai Vetter[a,c]

[a]Department of Nuclear Engineering, University of California, Berkeley, CA, USA
[b]Sandia National Laboratories, Livermore, CA, USA
[c]Lawrence Berkeley National Laboratory, Berkeley, CA, USA

Abstract

Spatial localization of special nuclear materials (SNM) via their neutron signatures amidst background requires knowledge of the background neutron environment or a means of separating a source from background based on low amounts of information. This requirement has created the need for characterizing the spatial distribution of the cosmogenic neutron background. Neutron scatter cameras have been developed and optimized for rapid detection of high activity sources, but have low imaging efficiency, making it difficult to use them to characterize low rate diffuse sources, such as the neutron background. The Low Intensity Neutron Imaging System (LINIS) is a collimated neutron imager that has been designed and optimized for imaging diffuse cosmogenic neutron background in the energy range of 0.5−15 MeV. LINIS operates using 16 liquid scintillation detectors shielded by ultra-high molecular weight polyethylene cylindrical collimators in a staggered orientation and rotates to 7 discrete positions, giving it roughly 2π sensitivity. LINIS has been characterized using (α, n) and fission neutron sources using two imaging techniques for neutron source localization, simple backprojection and Maximum Likelihood Expectation Maximization.

1. Introduction

Detection of special nuclear materials (SNM) via their neutron signatures is of specific interest due to a neutron's larger range and reduced self-shielding in the material in comparison to SNM gamma-ray signatures. There are also fewer naturally occuring neutron sources, making the geographic variability of the neutron background less significant when detecting SNM based on neutron signatures. ^{240}Pu, an example SNM of interest, undergoes spontaneous fission (SF) at a rate of 4.61×10^5 SF $\cdot$ s^{-1} $\cdot$ kg^{-1} [1] with an average yield of 2.151 n $\cdot$ SF^{-1} [2, 3]. This high neutron yield requires tens of centimeters to about a meter of material to shield to below background levels, making any shielded

Email addresses: adam_glick@berkeley.edu (Adam Glick), ebrubak@sandia.gov (Erik Brubaker), bcabrer@sandia.gov (Belkis Cabrera-Palmer), mgerlin@sandia.gov (Mark Gerling), eboado@berkeley.edu (Ethan S. Boado), kvetter@berkeley.edu (Kai Vetter)

container bulky. In contrast, highly enriched uranium (HEU) emits neutrons at a rate of less than $4\,s^{-1} \cdot kg^{-1}$ [4, 5] with an average yield of $2\,n \cdot SF^{-1}$. The neutron signatures released from SNM spontaneus fission events are weak compared to the gamma-ray signatures which adds a layer of complexity when localizing an SNM source based on the neutrons released.

Detecting and localizing HEU or ^{240}Pu that is shielded or at a standoff distance via neutron signatures may be limited by our understanding of the neutron background. This is due to the comparable rates and spectral features of SNM fission sources and the cosmogenic neutron background. Furthermore, the cosmogenic neutron background may vary with respect to time, geographical location, and the directions a neutron detector is sensitive to. This creates the need for a better way to measure and characterize the neutron background.

The neutron background spectral features have been investigated using Bonner sphere arrays [6], which showed that the detected spectrum below 5 MeV has an altitude, geomagnetic, and solar modulation dependence. These dependencies are strongest for neutrons with energies less than 1 MeV. A low pressure, time projection chamber filled with He and CF_4 performed a short surface measurement of the cosmogenic neutron background lasting 1.2 days [7]. The measurement collected only 16 identifiable neutron tracks and a preferential direction for the incoming cosmogenic neutrons based on the recoil tracks was undeterminable. Neutron background in urban Knoxville investigated using 8 EJ-301 liquid scintillation detectors found a 10% to 50% reduction in the observed neutron count rate compared with areas away from the downtown area, an effect found to be dependent on the 'angle-of-open-sky metric' [8]. This result was duplicated for the San Francisco/East Bay area when the Radiological Multi-sensor Analysis Platform (RadMAP) showed a correlation between the detected neutron count rates and the 'sky-view factor' (SVF) [9]. These building shielding metrics were then expanded upon using the Mobile Imager of Neutrons for Emergency Responders (MINER), a neutron scatter camera, which showed that the spatial distribution of the neutron background was modulated by the presence of urban buildings—where the neutron background source location was strongest in regions where buildings were not present [10]. The neutron background for which MINER was sensitive ranged in energy from 1.0 MeV to 12.7 MeV.

While these past measurements are all integral in understanding neutron background, each system mentioned only added partial information to the whole picture. Neither the Bonner sphere array nor RadMAP produced images based on the detected neutron background and focused only on the directionally independent aspects of their respective datasets. The measurement made with MINER produced images and spectral data from the neutron background, but with the low count rate that is intrinsic to neutron background and due to MINER's requirement for a double-scatter event to create a source location estimation, the statistics going into the reconstructions were too low to be able to produce high quality images of the spatial distribution of the diffuse neutron background [10].

The Low Intensity Neutron Imaging System (LINIS) was designed to overcome some of the limitations mentioned in [10] with regards to imaging the cosmogenic neutron background. Because of the spatial distribution of the neutron background shown in [10] being limited to the upper hemisphere of the imaging space, LINIS has been optimized to be only sensitive to the top ∼2π hemisphere. LINIS operates using 16 liquid scintillation detectors shielded by ultra-high molecular weight polyethylene (UHMWPE) cylindrical collimators in a staggered orientation and rotates to seven discrete positions, giving it roughly 2π sensitivity. Relative to MINER, this collimated design greatly increases the imaging efficiency by deriving spatial information from single interaction events, which will improve the quality of images for low rate diffuse sources produced with LINIS. This work describes the design and characterization of LINIS using neutron point sources to establish a baseline that may be used to interpret the results of future deployments where LINIS will be used to image the cosmogenic neutron background.

2. Collimated imager design

LINIS consists of 16 12.7 cm dia. × 12.7 cm tall cylindrical detectors filled with EJ-309 organic liquid scintillator. Several designs were considered that might improve the detection efficiency for low rate diffuse sources compared against the observed efficiency of MINER. These designs included several different geometries of scatter cameras using the 16 LINIS cells, such as a MINER configuration of cells based on a theory that the larger cell volumes might improve the double-scatter event efficiency. Each design was simulated in GEANT4Py [11] using the spectrum published in [6] for an energy range from the detection threshold energy of 0.5 MeV to 12 MeV. The metric used for comparison across the different designs was the number of imageable events resulting from the simulation using the same source type, position, and number of simulated events and the accuracy of the simple backprojection.

The design that was most efficient at imaging the simulated source was a collimated system of detectors using cylindrical polyethylene collimators to shield the detectors against neutrons coming from directions outside the opening of the collimators via attenuation. The collimated detectors had been optimized to scan the upper hemisphere of the imaging space by rotating about the central axis of system. Further optimization of the collimated design looked at different hydrogen rich materials that could function as collimators, yielding UHMWPE as the best candidate. The maximum cylindrical diameter of this material that could be ordered was 25.56 cm, which, after hollowing out to fit around a detector, left 5.91 cm of collimating material.

Simulations performed in GEANT4Py to investigate the attenuation capabilities of the UHMWPE material demonstrated that the fraction of neutrons interacting in the scintillators began to saturate at 15 MeV—that is to say that the fraction of neutrons depositing energy in the scintillators with and without the collimators in the beam's path began to approach equality at this energy. Considering the results from these simulations, the spectrum used to characterize

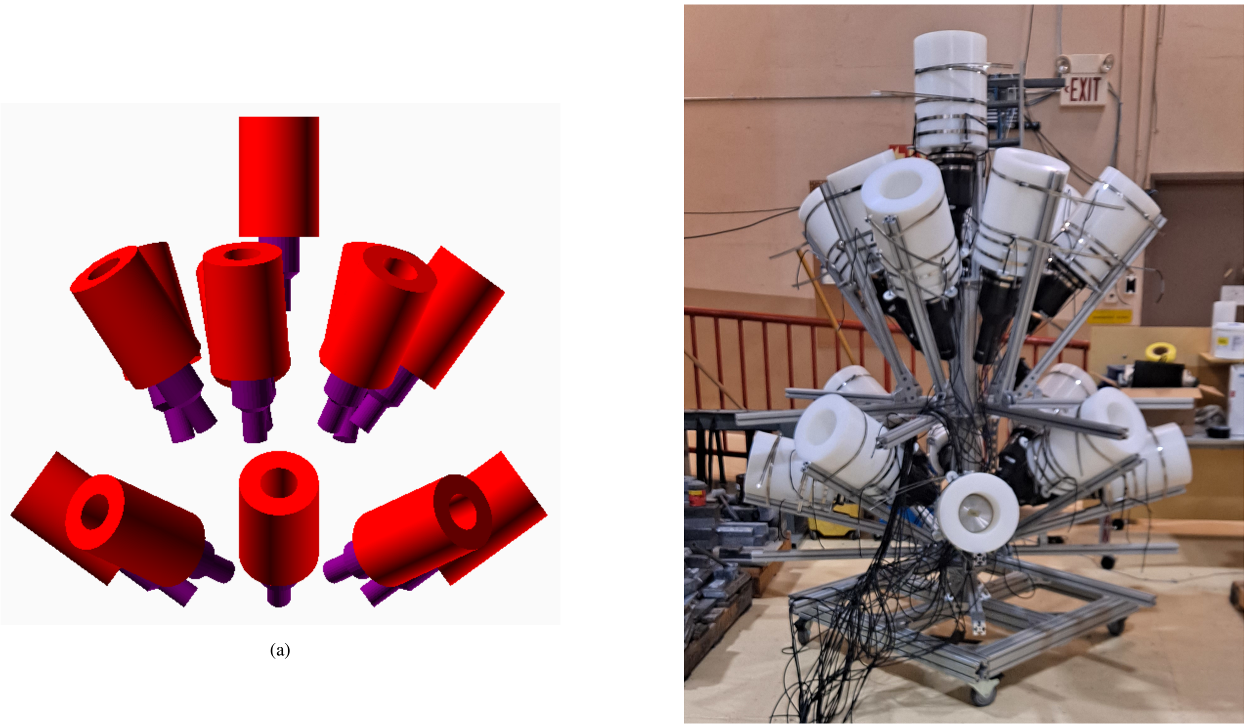

(a) (b)

Figure 1: (a) Computer-aided design model of LINIS system generated using OpenSCAD [12] shows staggered orientation of detectors in two rows (eight on the bottom row and seven on the top row) with a single detector pointing directly up. (b) The fully assembled LINIS shows 15 detectors in two rows (eight on the bottom and seven on the top) with one detector pointing directly upward. The detectors are situated on an aluminum frame that has wheels to allow for rotation and movement.

LINIS, taken from [6], was sampled for energies ranging from a detector threshold of 0.5 MeV up to 15 MeV, above the maximum energy that MINER was sensitive to.

The detectors are situated according to Fig. 1a where 1 detector points directly up and 15 detectors are pointed outward to maximize the elevation and azimuthal coverage of the imaging space. Although designed to have 16 detectors total, a malfunctioning PMT leaves LINIS with only 15 working detectors. The broken detector was placed at the location on LINIS that would overlap the most with other detectors, allowing LINIS to retain its $\sim 2\pi$ sensitivity.

The detectors are situated on an aluminum frame, chosen to minimize the interactions of background neutrons in the support material. Fig. 1b shows the full system where the detectors are held at the correct positions using support braces, pivot arms, and hose clamps. Each of the two rows are held in position using custom circular 306 stainless steel discs. LINIS is a modular system where the collimators can be removed, allowing LINIS to operate as a kinematic detector, so that the background spectrum, convolved with LINIS's energy resolution, can be determined from neutron double-scatter events.

3. Data processing

The cells are calibrated using a ^{22}Na source to convert from arbitrary digitizer units to energy in MeVee. The proton recoil kinetic energy E_p, expressed in MeV, was obtained from the the measured light output L, in MeVee, by inverting the function

$$L = 4.87 \times 10^{-2}\,\mathrm{MeVee/MeV^2} \cdot E_p^2 + 4.50 \times 10^{-2}\,\mathrm{MeVee/MeV} \cdot E_p + 3.70 \times 10^{-5}\,\mathrm{MeVee}\,. \tag{1}$$

The coefficients in Eqn. (1) were determined for EJ-309 and published in [10]. Eqn. (1) is used to determine the lowest proton recoil energy that LINIS can detect corresponding to the detection threshold in MeVee units.

3.1. Particle identification using pulse shape discrimination

Pulse shape discrimination (PSD) was used to classify interacting particles as either neutrons or gamma rays using a Bayesian approach [13]. The PSD parameter value was calculated as the ratio of the total waveform integral after baseline subtraction, representing the prompt and delayed fluorescence, and the prompt-only integral. Since neutron interactions produce more delayed fluorescence in organic scintillators, their corresponding PSD band has higher average PSD parameter values than gamma rays. This can be observed in Fig. 2 where observed neutrons populate the band with higher PSD values and observed gamma rays populate the band with lower PSD values.

Taking vertical slices through the PSD bands creates a set of one-dimensional distributions, each of which can be fit by two Gaussian curves that have the form

$$f_{i,E_k}(s) = \frac{1}{\sigma_{i,E_k}\sqrt{2\pi}} \exp\left(-\left(\frac{s-\mu_{i,E_k}}{\sqrt{2}\sigma_{i,E_k}}\right)^2\right), \tag{2}$$

where s is the PSD value, i is the particle type, and E_k represents the energy bin that the vertical slice is taken at. A Radial Basis Function [14] interpolation is performed on the average, μ, and standard deviation, σ, of the PSD distributions as a function of electron-equivalent energy in MeVee.

The μ and σ fits are used to calculate the probability for a detected particle to be a neutron or gamma ray as

$$P(n|s) = \frac{f_{n,E_k}(s)}{f_{\gamma,E_k}(s)w_{\gamma/n} + f_{n,E_k}(s)} \tag{3}$$

through an iterative process. $P(n|s)$ is the probability of a particle being a neutron given a PSD paramter value, s, f is the Gaussian defined in Eqn. (2) for neutron and gamma ray distributions, and $w_{\gamma/n}$ is the ratio of the estimated number of events in the gamma-ray and neutron distributions within an energy bin which is used as a weight to calculate the posterior probabilities. The weight $w_{\gamma/n}$ is assumed to be unity on the first iteration and is updated each iteration such that

$$w_{\gamma/n} = \frac{\sum_{s \in E} P(\gamma|s)}{\sum_{s \in E} P(n|s)}, \tag{4}$$

where $P(\gamma|s)$ is the probability of a particle being a gamma ray, having a similar form to Eqn. (3). The neutron probabilities, gamma ray probabilities, and weights are updated each iteration until the change in $w_{\gamma/n}$ between two consecutive iterations is less than 1%.

The resulting PSD bands can be seen in Fig. 2 with data collected in the presence of a ^{252}Cf fission source, where there is clear separation for energies above 0.25 MeVee and significant overlap for lower energies. The purple lines lines represent the mean neutron and gamma ray PSD values as a function of energy and the black lines represent the $\pm 1\sigma$ widths. Because the UHMWPE collimators cannot effectively attenuate gamma rays, this work uses a strict 99.95% neutron acceptance probability to minimize the contribution of gamma rays to the image. The resulting neutron band is bounded by the dashed red line seen in Fig. 2. We define the effective threshold for a cell as the energy at which the average neutron fit (upper purple line) and the 99.95% neutron acceptance boundary (lower dashed red line) intersect. This occurs at 0.165 MeVee for the data displayed in Fig. 2, corresponding to a proton recoil energy of 1.44 MeV. Each cell has slightly different performance; the mean and standard deviation of the effective threshold across all detector cells were 1.34 MeV and 0.36 MeV, respectively, expressed here as proton recoil energy. For larger PSD values it is possible to classify neutrons with energies less than where these two bands cross, however, as seen by the vertical line that bounds the neutron acceptance region in Fig. 2, there is an energy threshold below which events cannot be classified as neutrons with the necessary confidence.

4. Collimated image reconstruction

With the collimated imager design, directional information for the origin of detected neutrons is contained in single interaction events, which can be used to estimate the source location through simple backprojection or a more sophisticated maximum likelihood expectation maximization reconstruction. These methods for image reconstruction will be discussed in this section along with simulations and experiments performed that increase the accuracy of each source location estimation method.

4.1. Simple backprojection

Collimated imaging uses collimating material surrounding a detector to enhance its sensitivity to events coming from the opening in the collimator. Fig. 3a depicts a diagram of how the collimator is situated around a detector as

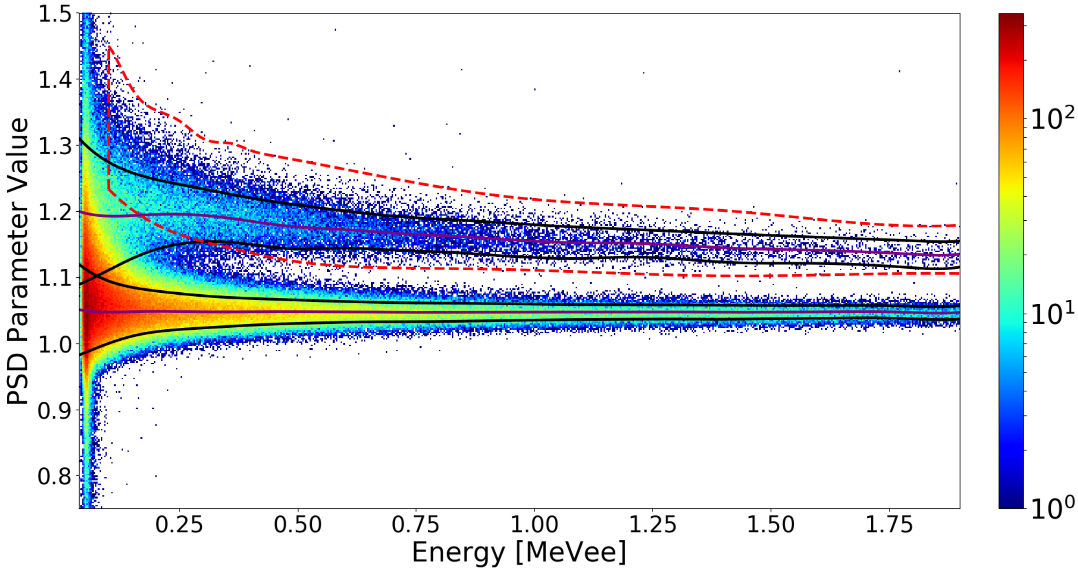

Figure 2: PSD heatmap for data collected with a single detector at a single rotation as a function of electron-equivalent energy in MeVee showing low density of neutrons (top band) and high density of gamma rays (bottom band). The purple lines represent the mean neutron and gamma ray PSD values as a function of energy and the black lines represent the $\pm\ 1\sigma$ widths. The dashed red line bounds the region where events are classified as neutrons with a 99.95% probability.

well as the solid angle for which a detector is sensitive. For a perfectly attenuating cylindrical collimator, the detectors are sensitive to neutrons coming from directions defined by a solid cone with opening angle

$$\theta = \tan^{-1}\left(\frac{r}{\ell}\right), \tag{5}$$

where $\ell = 29.21$ cm is the distance from the center of the detector to the end of the collimator and $r = 6.35$ cm is the radius of the detector. The axis of this solid cone is defined as the unit directional vector $\hat{\omega}$, which is determined by the detector's polar and azimuthal orientations, referred to hereafter as the detector's tilt. This is a first order approximation and does not account for the finite extent of the detector as depicted in Fig. 3a.

To further understand the angular sensitivity of the collimated detectors in the realistic case of collimating material with finite attenuation, a simulation was performed in GEANT4Py. A pencil beam of neutrons that covered the entire detector, collimator, and PMT was positioned about the center the detector and scanned through a range of incident angles. The neutron spectrum used in this simulation was sampled from [6] and the resulting normalized fraction of detected neutrons as a function of incident angle can be seen in Fig. 3b. The angular response up to 30° appears Gaussian and has a full width at half max, defined as twice the beam angle where the half maximum occurs, of 32.5°. The data generated in GEANT4Py up to 30° was reflected about 0° and fit with a Gaussian curve. The fit intersects all

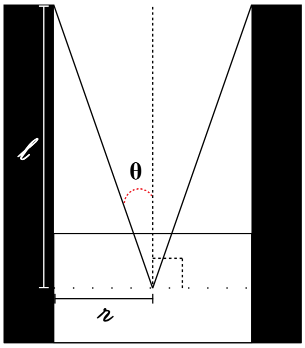

(a)

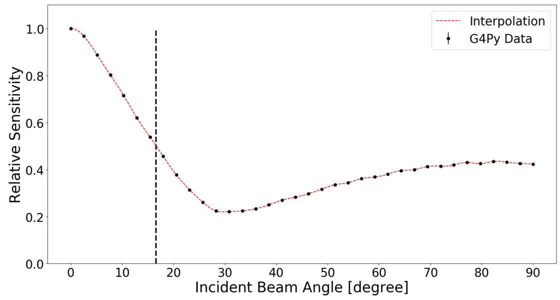

(b)

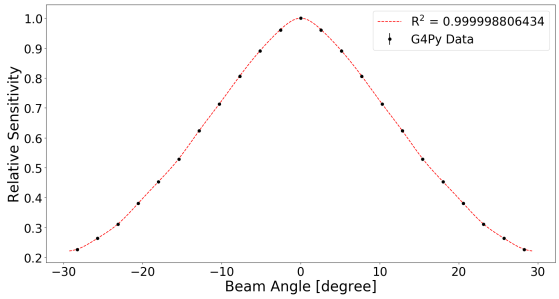

(c)

Figure 3: (a) Diagram depicting a collimator (black region) surrounding a detector defined by the boxed region at the bottom of the diagram. A solid cone is projected out from the center of the detector with cone angle θ, defining the area where the detector is sensitive to neutrons. (b) Normalized angular sensitivity of a single detector surrounded by a collimator, as seen in Fig. 3a, as a function of incident beam angle for the neutron spectrum in [6]. The black dots are the relative number of particles detected at each beam angle and the dashed red line is the Radial Basis Function [14] (RBF) interpolation of the data. The vertical line intersects the interpolation at the FWHM, 16.4°. (c) Angular resolution of a collimated detector reflected about the 0° axis and fit with a Gaussian shows good agreement between the data and the approximation ($R^2 \approx 1$). The FWHM of this Gaussian is 32.5° which gives an angular resolution for a single detector σ_c equal to 13.8°.

data points within their uncertainty and has a correlation coefficient (R^2) value, a metric for determining the closeness of a fit with data, of ~ 1.0 as seen in Fig. 3c. The angular resolution of a single detector can be defined in terms of the standard deviation of the Gaussian, σ_c, as $\mathrm{FWHM}/\left(2\sqrt{2\ln 2}\right)$, equal to 13.8°. The relative sensitivity up to a beam angle of 30° is similar to a Gaussian due to the amount of opening the collimator has in the beam's eye view; beyond that the sensitivity changes according to the amount of collimating material a neutron has to go through to interact in a detector.

While the Gaussian approximation includes the partial angular response of the collimated detectors omitted by the opaque approximation defined by Eqn. (5), capturing the angular sensitivity of a collimated detector beyond 30° requires a more sophisticated imaging methodology. Despite its limitations, the location estimation for a neutron source that is obtained using the Gaussian approximation has shown good agreement with these more sophisticated methods, as will be discussed below, and is primarily used as a sanity check that validates the estimation obtained using a system response.

A simple backprojection image is constructed on the upper hemisphere of the unit sphere, which is divided into 5,460 equal-area bins using the HEALPix [15] package. The unit vector pointing to the center of a given bin is $\hat{\varepsilon}$. For an imager with D' detectors that rotates around its central axis to R' discrete positions, the number of events observed by each detector at each system rotation is used to scale the corresponding solid cone, resulting in the backprojected image $b_c(\hat{\varepsilon})$ given by

$$b_c(\hat{\varepsilon}) = \frac{1}{S_c} \sum_R \sum_D M_{D,R} \left(H\Big(\hat{\varepsilon} \cdot \hat{\omega}_{D,R} - \cos(\Theta)\Big) \exp\left(- \left(\frac{\hat{\varepsilon} \cdot \hat{\omega}_{D,R} - \cos(0)}{\sqrt{2}\bar{\sigma_c}} \right)^2 \right) \right), \tag{6}$$

where $M_{D,R}$ is the number of events observed in detector $D \in [0, D']$ at rotation $R \in [0, R']$, $\bar{\sigma_c} = \cos(0) - \cos(\sigma_c)$ is the standard deviation of the angular sensitivity in cosine space, $\Theta = 30°$ bounds the Gaussian approximation from the center of the 2D distribution, and H is the heaviside step function which has the form

$$H(x) = \int_{-\infty}^{x} \delta(s) ds = \begin{cases} 0 & x < 0 \\ \frac{1}{2} & x = 0 \\ 1 & x > 0 \end{cases}. \tag{7}$$

The scaling factor $1/S_c$, where

$$S_c = \sum_R \sum_D \rho_D \left(H\Big(\hat{\varepsilon} \cdot \hat{\omega}_{D,R} - \cos(\Theta)\Big) \exp\left(- \left(\frac{\hat{\varepsilon} \cdot \hat{\omega}_{D,R} - \cos(0)}{\sqrt{2}\bar{\sigma}} \right)^2 \right) \right), \tag{8}$$

represents a geometric bias function that corrects regions of space where the simple backprojection is biased toward. The image is biased toward these regions due to overlapping cones at multiple rotation positions, such as the vertical detector adding its events to the same source bins at every rotation. Detector efficiency is considered in this backprojection method by scaling the projected cones from detector D with the relative efficiency of the detector, ρ_D.

To measure the relative differences in PSD efficiency among the 15 functional detectors, an experiment was performed that placed a ^{252}Cf neutron source 1.75 m from the center of each collimated detector. Neutrons were collected for several minutes and the relative number of observed neutrons was determined using the 99.95% neutron acceptance threshold on Eqn. (3). The relative PSD performance for each detector, ρ_D, can be seen in Fig. 4. The geometric bias function for LINIS with detectors $D \in [0, 14]$ can be seen in Fig. 5a for the $R = 0$ rotation and in Fig. 5b for all rotations $R \in [0, 6]$.

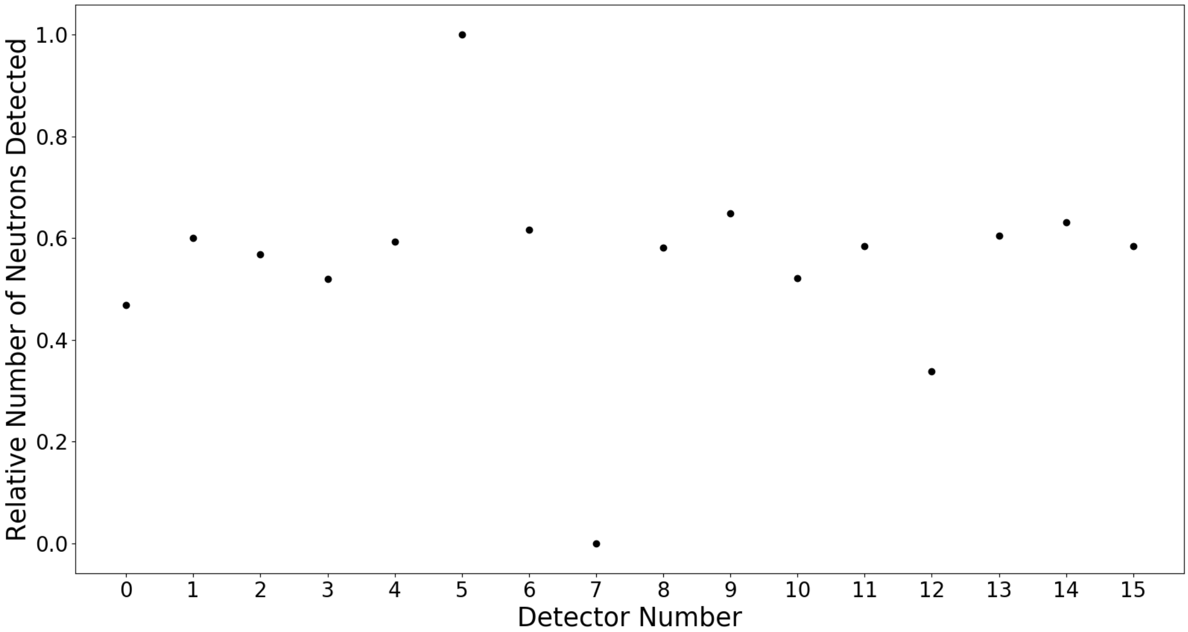

Figure 4: Relative number of neutrons observed across all 16 detectors using a ^{252}Cf fission source placed 1.75 m from the center of each detector.

4.2. Maximum Likelihood Expectation Maximization

To take into account finite attenuation of the collimators, scattering off of the support frame, non-Gaussian angular sensitivity, and other factors not represented in Eqn. (6), a better representation of neutron source locations can be reconstructed using Maximum Likelihood Expectation Maximization (MLEM) [16]. MLEM uses a model of the system generated in GEANT4Py to iteratively update an estimation for the spatial distribution of the source corresponding to the ensemble of observed events as

$$\lambda_a^{(k+1)} = \frac{\lambda_a^{(k)}}{\sum_i^N C_{a,i}} \sum_i^N \frac{n_i^* C_{a,i}}{\sum_{a'}^A \lambda_{a'}^{(k)} C_{a',i}}, \tag{9}$$

where n_i^* is the measured data distributed over $i = 1, 2, ..., N$ discrete observations, $C_{a,i}$ is a matrix that lists the probability of an event observed in observation bin i originating in source bin a at location (θ, ϕ), and $\lambda_a^{(k)}$ is the estimation of the intensity neutrons at spatial location a on the k-th iteration. This estimation is then normalized by dividing by the sensitivity of the system — the sum of $C_{a,i}$ over all observation bins i — to prevent the image from biasing to regions of high sensitivity. For systems that have very uniform sensitivity across all source locations, the sensitivity correction is not needed to reconstruct the image. The sensitivity for LINIS is seen in Fig. 6 where it has roughly uniform sensitivity to neutrons across azimuthal angles in the upper hemisphere with an azimuthally modulated sensitivity between 60°−90° in elevation. The observation bin is defined as the rotation of the system and

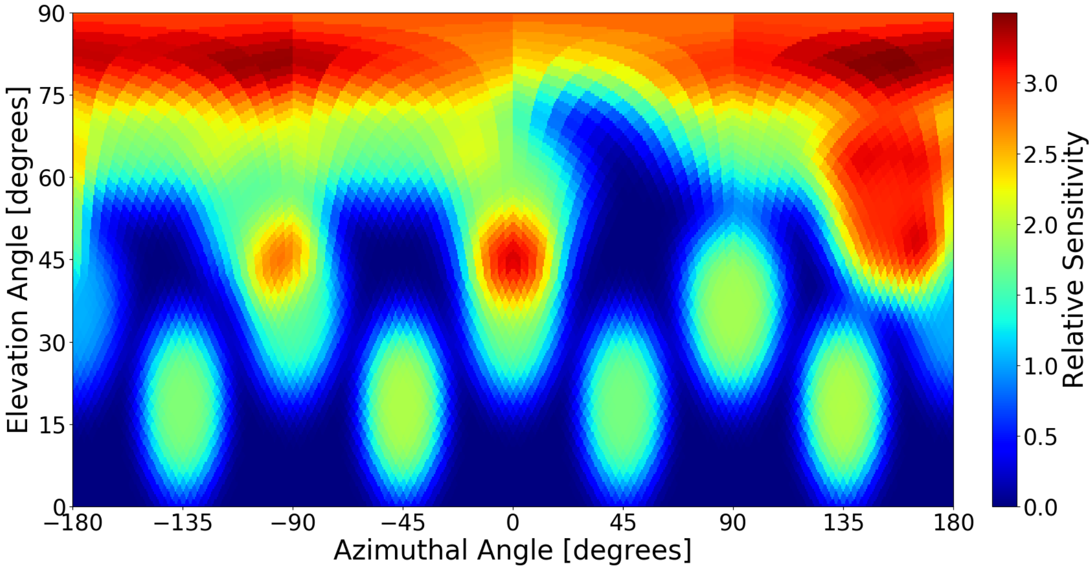

(a)

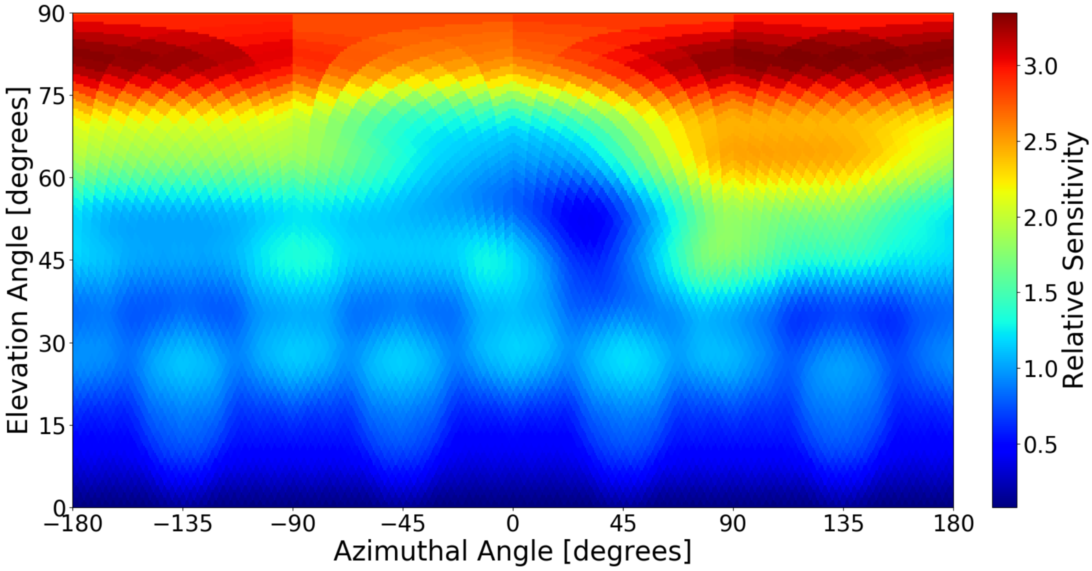

(b)

Figure 5: (a) Geometric bias function for a single rotation shows the position of each of the eight detectors on the lower row, where the seven detectors on the higher row have significant overlap and the solid cones cannot be completely resolved. (b) Geometric bias function for all rotations shows higher relative sensitivity in the regions where solid cones projected from nearby detectors overlap and lower sensitivity in the regions where the detectors equally cover the imaging space.

the detector that observed the event. The system has seven discrete azimuthal rotation positions ($R \in [0, 6]$) in 15° increments to cover the $\sim 2\pi$ imaging space that LINIS is sensitive to. The simulation to generate the LINIS system response is discussed in detail below.

The response matrix for this system was built using a direct Monte Carlo approach in GEANT4Py. The geometry for LINIS was built to include the support frame, collimators, detectors, and a 15.24 cm thick concrete floor directly below LINIS modeled as a 20 m × 20 m × 15.24 cm rectangular prism. A cone beam of neutrons that covered the full system and had a continuous energy distribution was simulated at 5,460 source locations for elevation angles $\phi \geq 0$ defined with HEALPix binning. Multiple interactions within each cell, scattering within collimators, between detectors, off the aluminum frame, and off of the concrete floor as well as the finite attenuation of the collimators are accounted for as a result of the geometry included in the simulation. Variable angular sensitivity for each detector relative to different azimuthal and elevation source locations and additional shielding provided by other detectors are also accounted for in this model which are not included in the simple backprojection. With care for detection thresholds, the absolute probability for each observation/source bin pair was determined for an energy spectrum definied by the neutron background spectrum published in [6]. The response matrix was modified to change all observation bins corresponding to the malfunctioning detector such that they did not add to the total LINIS response during MLEM reconstruction, however its contribution as a shielding and scattering object for other detectors remained. Each observation/source bin pair was then corrected for PSD by multiplying the absolute probability by the associated detector's relative PSD efficiency, shown in Fig. 4.

This simulation was only performed for the $R = 0$ rotation to determine the probability for each observation/source bin pair. Since the location of the detectors with respect to each other and to the frame is the same for all rotations, the observation bin probabilities for the six other rotations were determined by matching the calculated observation bins with their corresponding source bins at each new rotation.

When using MLEM, a common issue is when to stop iterating the data through the system response matrix. A multitude of ideas have been proposed such as 'Poisson feasibility' [17] where iterations end when the result appears Poisson after inclusion of a noise factor and 'Monte Carlo agreement' [18] where iterations stop when the result has good agreement with Monte Carlo simulations. These types of stopping criteria depend on a priori knowledge about the data, which may not always be the case. Therefore, this work uses a stopping criteria that is independent of any a priori knowledge, defined as

$$\xi^{(k+1)} = 1 - \frac{\sum_{a'}^{A} \left(\lambda_a^{(k+1)} - \overline{\lambda_a^{(k+1)}}\right)\left(\lambda_a^{(k)} - \overline{\lambda_a^{(k)}}\right)}{\sum_{a'}^{A} \left(\lambda_a^{(k+1)} - \overline{\lambda_a^{(k+1)}}\right)\left(\lambda_a^{(k+1)} - \overline{\lambda_a^{(k+1)}}\right)}, \tag{10}$$

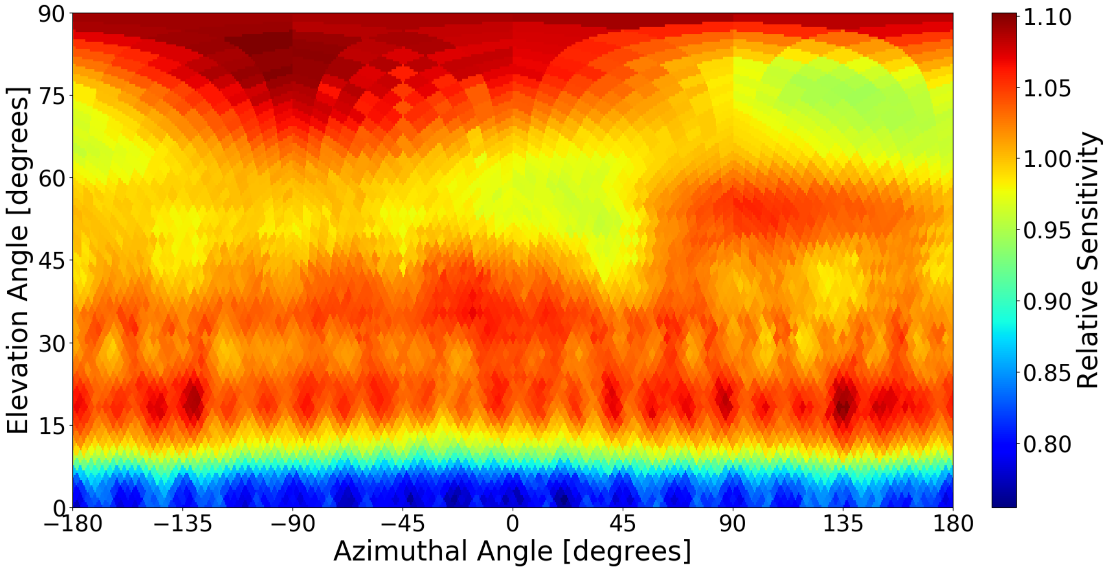

Figure 6: Sensitivity of the LINIS system shows nearly uniform azimuthal coverage in the northern hemisphere of imaging space. The azimuthally modulated shape in the sensitivity between 65°−90° is due to nonuniform coverage of the imaging space. Additional rotations would smooth out this shape, but would cause the loss of statistics at each individual rotation position.

where $\lambda_a^{(k+1)}$ is the forward projection of the data on the current iteration and $\lambda_a^{(k)}$ is the forward projection of the data on the previous iteration. $\xi^{(k+1)}$ estimates the divergence of the source distribution estimation on the current iteration from the source distribution at the previous iteration. In the limit as $k \to \infty$, $\xi^{(k+1)} \to 0$. Plotting Eqn. (10) as a function of iteration creates three separate regions, A, B, and C, separated by the maximum and inflection point of $\xi^{(k+1)}$ as seen in Fig. 7.

These regions have been analyzed using data taken with LINIS and the trajectory of the image in each of these three regions has been determined heuristically rather than by first principles. In region A, the estimation is improving lower frequency aspects of the image up to the maximum of the curve. After the maximum in region B the estimation begins to improve the higher frequency components of the image and the estimation converges towards the source bins of highest probability for the true source location. Region B ends at the inflection point, $\mathrm{d}^2\xi^{(k+1)}/\mathrm{d}k^2 = 0$, when the image begins to pixelate along the curve in region C. The MLEM algorithm is stopped at this point in which the convergence of the estimation is at a maximum without overfitting.

5. System characterization measurements

In order to characterize LINIS's angular resolution and sensitivity for neutron imaging, two neutron point sources, PuBe and ^{252}Cf, were used in three different experimental configurations described in Table 1. The PuBe source was

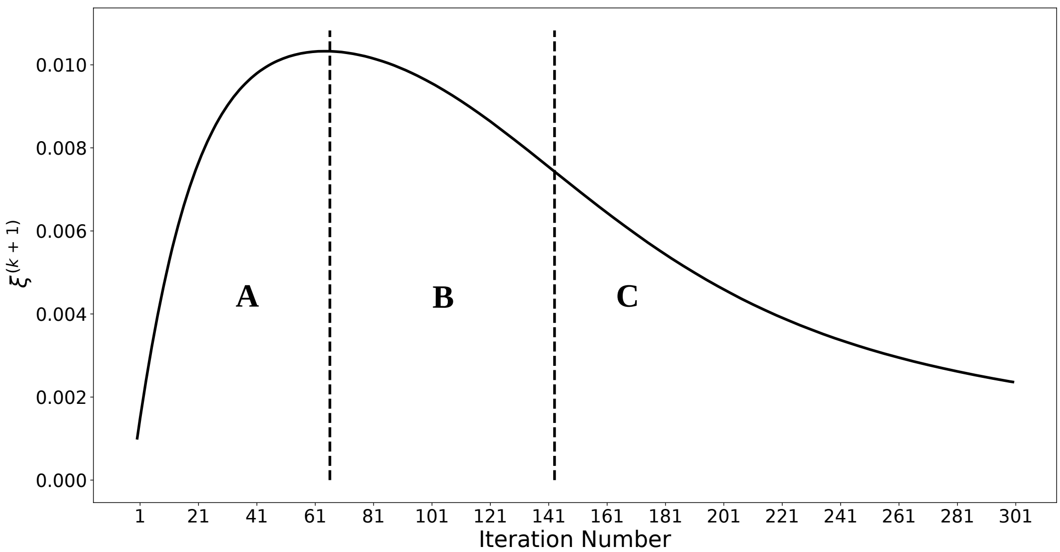

Figure 7: Eqn. (10) graphed as a function of iteration number, k reveals three distinct regions representing low frequency improvement (region A) which occurs between the second full MLEM iteration ($k = 1$) and the maxima where $\mathrm{d}\xi^{(k+1)}/\mathrm{d}k = 0$, high frequency improvement (region B) which occurs between the maxima and the inflection point where $\mathrm{d}^2\xi^{(k+1)}/\mathrm{d}k^2 = 0$, and pixelation (region C) which occurs for iterations above the inflection point.

1 Ci, producing between 1.5 and $2 \times 10^6\,\mathrm{n \cdot s^{-1}}$, and the ^{252}Cf source was $500\,\mu$Ci, producing $2.2 \times 10^6\,\mathrm{n \cdot s^{-1}}$. The first configuration placed a ^{252}Cf fission source at a high elevation to test the ability of the system and response matrix to correctly localize a source at an elevation near the region of space where cosmogenic background neutrons are expected to be originating. The detected neutrons for the ^{252}Cf placed at 54° elevation were used to create a simple backprojection according to Eqn. (6) leading to the image in Fig. 8 and to estimate the source location using the system response by a single iteration of Eqn. (9) as seen in Fig. 9a. In both images, the source location is estimated at the correct position of 0° azimuthal 54° elevation with blurring around the rest of imaging space. Fig. 9a was then iterated through Eqn. (9) 142 times to improve the source location estimation, with the stopping condition defined as the inflection point of Eqn. (10), as described above. As seen in Fig. 9b, the source location estimation converges to the true source location with an artifact in the high elevation region of the image. The source of this artifact may be related to LINIS's increased sensitivity to sources located at high elevations. With less data going through the MLEM process, statistical fluctuations in the observation space can cause estimations for the source location to increase in regions of high sensitivity. Two additional artifacts can be seen in both the collimated cone backprojection and the MLEM images at azimuthal angles of −90° and 140°. These artifacts have low intensity compared to the hotspot and may be due to finite attenuation of the collimators, scatting events in surrounding concrete support pillars in the lab that were not included in the simulation, or some other origin. Because of presence of these artifacts in the collimated

Figure(s)	Source(s)	Elevation	Azimuth	Distance	Height
8–9	^{252}Cf	54°	0°	3.00 m	4.17 m
10	PuBe	12.8°	0°	5.99 m	1.37 m
11	PuBe	15.86°	-130°	9.30 m	2.64 m
	^{252}Cf	12.30°	−138.75°	12.12 m	2.64 m

Table 1: Neutron source types and locations used to characterize LINIS.

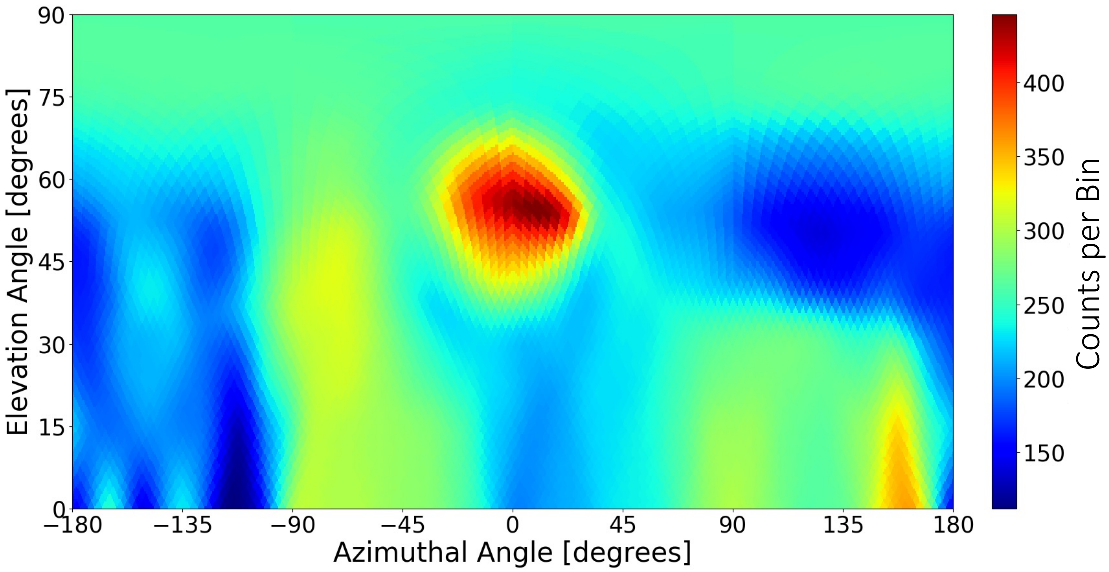

Figure 8: Simple backprojection approximation of 8.55×10^5 events from a ^{252}Cf source positioned at 54° elevation and 0° azimuth using Eqn. (6).

cone backprojection, it is clear that these artifacts do not arise simply due to the LINIS response matrix. Despite these features, the highest probability for the source location of the observed neutrons corresponds to the known location of the ^{252}Cf source. This agreement between two imaging techniques with a known source location verifies the accuracy of the GEANT4Py simulated system response for measurements made with LINIS.

The second source location was chosen to be a region of low relative sensitivity and to test LINIS's ability to localize a source near a highly scattering object, in this instance the concrete lab floor. The source was placed at a position of 0° azimuthal 12.8° elevation. The data was iterated through Eqn. (9) 109 times to generate Fig. 10a, in which the estimation converges to the true location of the neutron source. A modulated feature at high elevations centered about the azimuthal location of the source is present, possibly due to LINIS' higher sensitivity at these

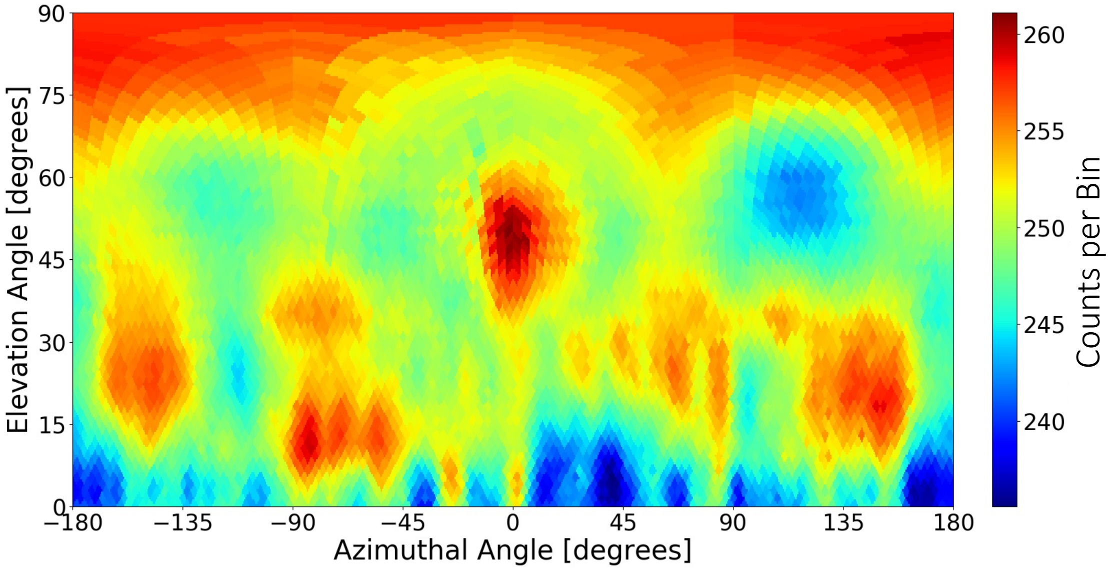

(a)

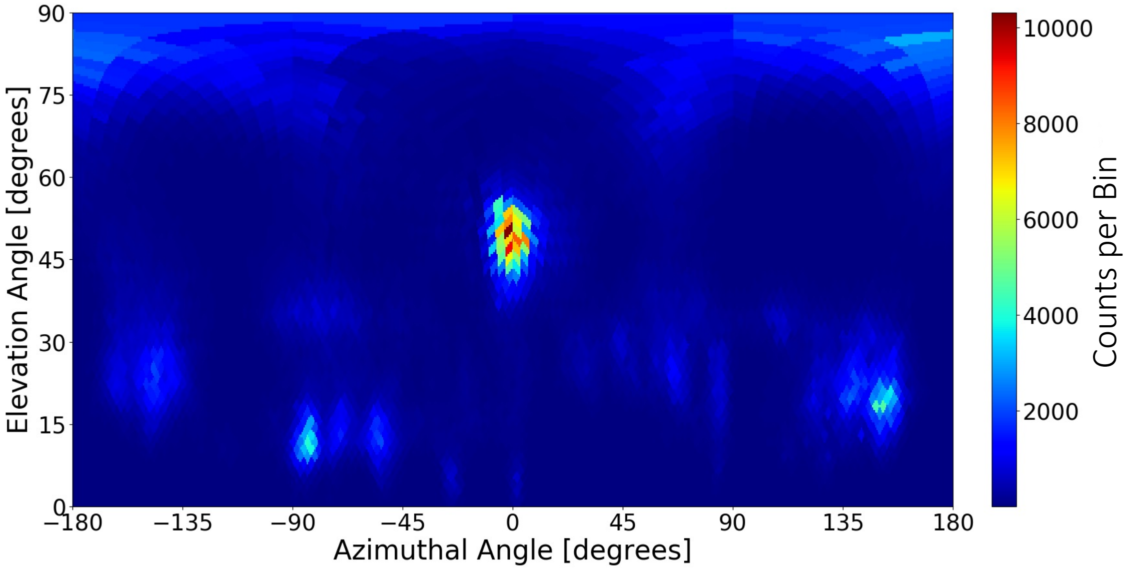

(b)

Figure 9: (a) First MLEM source location estimation of ^{252}Cf source positioned at 54° elevation and 0° azimuth projecting 8.55×10^5 events through Eqn. (9). (b) 142nd iteration estimation of a ^{252}Cf source location while positioned at 54° elevation and 0° azimuth using Eqn. (9).

elevation.

To investigate the capability of LINIS to detect a low intensity source, this time-sorted data was randomly down sampled to 0.5% of the total number of events to generate new observation data. The randomly down-sampled data was projected through the LINIS response matrix 77 times to produce the source distribution observed in Fig. 10b. The MLEM estimation of the neutron source location still converges toward the true location, but the high elevation feature is more prominent than in Fig. 10a due to the limited amount of data going through the MLEM procedure resulting in a higher estimation for the source location being attributed to LINIS's highest sensitivity. It is also noteworthy that while most downsampled datasets produced images similar to Fig. 10b, at this high degree of downsampling some datasets produced images that did not converge to the correct location due to statistical fluctuations changing the order of the measurement in different observation bins.

The final location chosen was intented to test LINIS's detection capabilities for an off-axis source while simultaneously determining if LINIS could localize two sources separated by less than a single detector's angular resolution. PuBe and ^{252}Cf sources were placed apart by 9.45° total and data was collected at each rotation position. The data collected was iterated through Eqn. (9) 94 times where the source location estimation converges toward the region of space where both sources were located. Fig. 11 reveals that LINIS can localize the spatial location of the sources at an off-axis position, but it appears to not be able to separate the two sources from each other.

5.1. Shielded source measurement

LINIS was used to measure the background in the laboratory after the sources had been placed in their shielded containers and stored in a locked vault with concrete walls. Data was taken for 2 hours at each rotation position for a total of 14 hours. The PSD fits calculated in Section 3.1 were necessary due to the limited number of neutrons observed in comparison to the gamma rays, as can be seen in Fig. 12. The neutron band has higher PSD values than the gamma-ray band and the selected neutron data is bounded by the dashed red lines for a single detector at a single rotation.

The selected neutrons using Eqn. (3) were projected through the response matrix using Eqn. (9). The first source location estimation, seen if Fig. 13a, shows that neutrons are estimated to be coming primarily from low elevations, a result that would suggest cosmogenic background neutrons were not observed since it was observed in [10] that the neutron background is primarily originating at higher elevations. This can be explained by the location of LINIS in the laboratory being underneath six floors of concrete, which was shielding the background neutrons coming from cosmic-ray spallation reactions. Additionally, the region of highest intensity in the image corresponds to the location of the shielded sources in the concrete vault. A higher elevation feature can be observed at similar azimuthal angles as the low elevation hotspots, potentially due to the overlap of detectors scanning those areas of space.

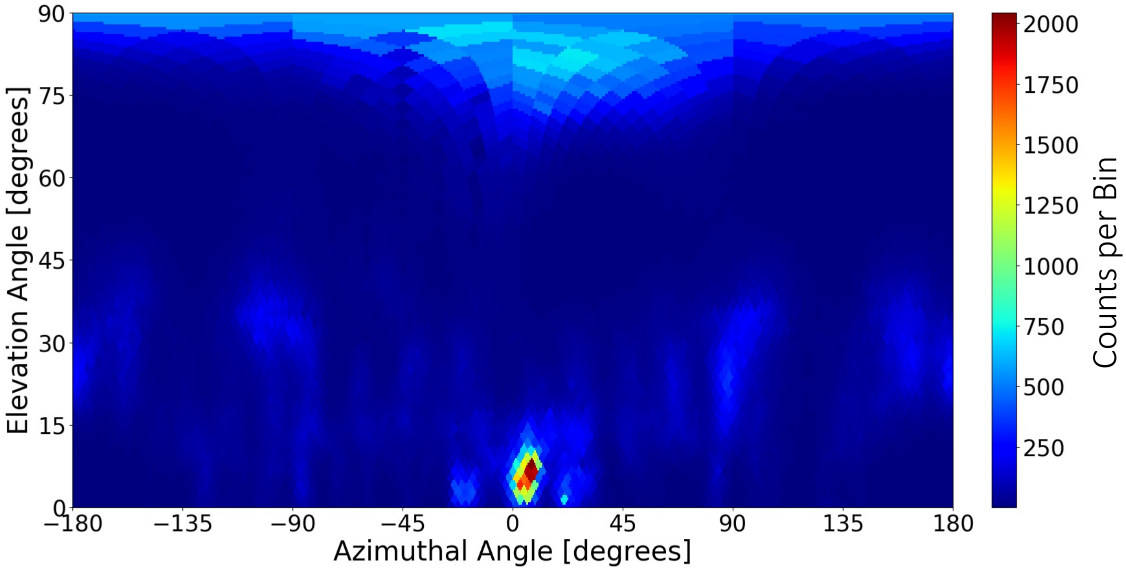

(a)

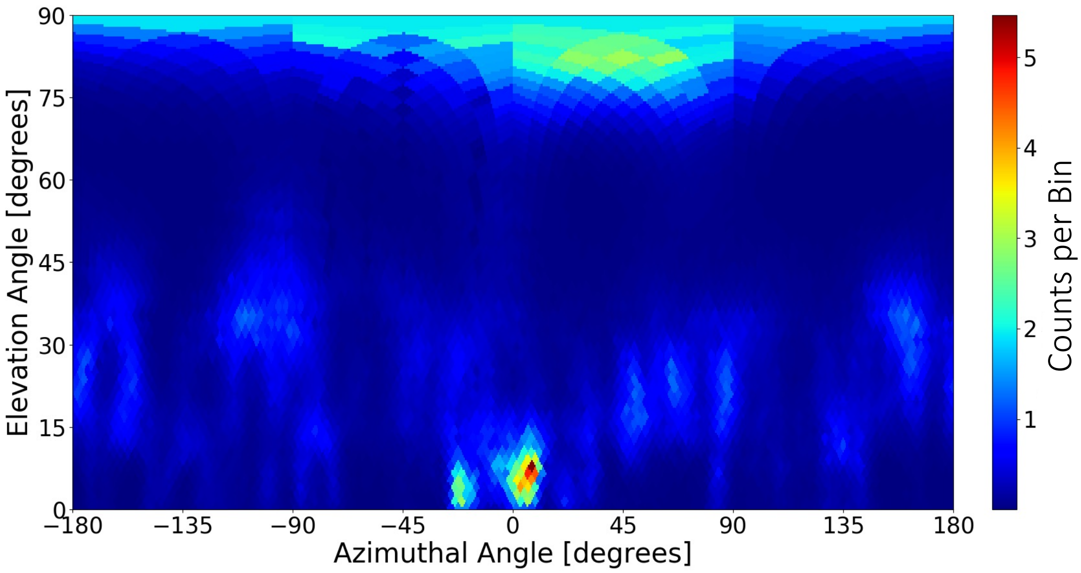

(b)

Figure 10: (a) 109th iteration estimation of neutron source location using Eqn. (9) with 3.29×10^5 observed events. (b) 77th iteration estimation of neutron source location after downsampling the data to 1.64×10^3 observed events still converges to near the true source location, but due to LINIS's higher sensitivity at higher elevations, more neutrons are estimated to be originating at these regions of space when less data is projected through the response matrix.

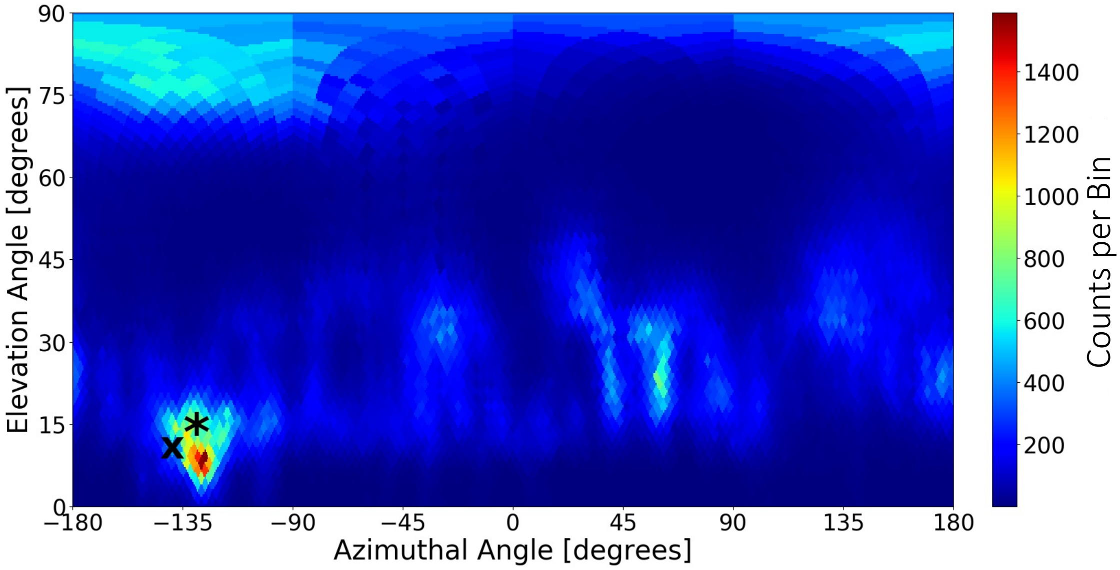

Figure 11: 94th iteration estimation produced when a total of 5.75×10^5 neutron events detected from ^{252}Cf and PuBe neutron sources with (ψ, ϕ) locations listed in Table 1 that are separated by 9.45° is passed through the LINIS response matrix to create improved source location estimations. The PuBe source is marked by the "✱" and the ^{252}Cf source is marked by the "✕". Estimation of PuBe and ^{252}Cf neutron source locations using Eqn. (9) converges to their location, but the two sources cannot be completely resolved.

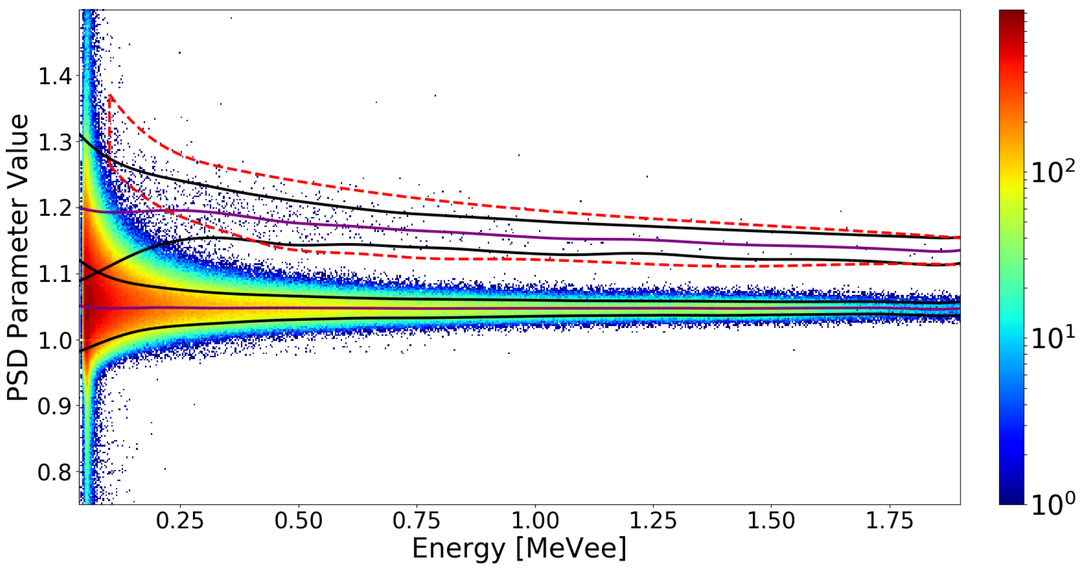

Figure 12: PSD plot as a function of electron-equivalent energy in MeVee. The purple lines correspond to the mean PSD fits for neutrons and gamma rays and the black lines correspond to the $\pm 1\sigma$ deviations from the means. The neutron band from background data is significantly limited in comparison to when a source is present in Fig. 2.

The collected background data was iterated through Eqn. (9) 99 times to improve the source location estimation. Fig. 13b reveals the resulting image where the estimation converges towards the location of the vault where the two shielded neutron sources are stored. Interestingly, the convergence of this image using the metric defined by Eqn. (10) allows both sources to be observed separated by 22.4°. While the actual locations of the sources were not recorded for this background measurement, the separation of the sources was significantly larger than in Fig. 11 based on the best recollection of the experimenter. The high elevation feature remains, perhaps due to the low number of events observed from the sources under these conditions. Based on the result of the downsampled data in Fig. 10b, this feature is not unexpected. While the high elevation features may degrade the system resolution when imaging background neutrons coming preferentially from higher elevations, the lack of such a feature when imaging the high elevation source in Fig. 9b gives confidence that this feature will not affect LINIS's ability to image cosmogenic neutron background. The convergence of the estimation toward the region of space where the shielded sources are stored emphasizes LINIS's ability to localize background level neutrons.

6. Conclusions

The design and performance of the collimated fast neutron imager LINIS has been described above that has $\sim 2\pi$ sensitivity in the upper hemisphere of the imaging space. LINIS has been optimized for localization of neutrons based on a low number of detected events – the ultimate goal being to image diffuse cosmogenic neutron background – and its ability to do this has been displayed in Figs. 10b and 13b.

Although not described in this work, LINIS may function as a neutron scatter camera when its collimators have been removed. This will allow the system to collect spectral data when deployed for background measurements. It is also possible to add an energy dimension to the LINIS response function to unfold an energy spectrum from the observed data.

The system presented here will be deployed in urban environments to collect spatial information on background neutrons produced from cosmic ray spallation. It will be used to investigate the results in [10] on the modulation of the spatial distribution of neutron background by urban buildings. While LINIS has proven capable at imaging point sources using the techniques described above, it remains an open question how well these techniques will perform in the mission to image diffuse cosmogenic background.

Acknowledgments

This material is based upon work supported by the U.S. Department of Homeland Security under Grant Award Number, 16DNARI00026. Sandia National Laboratories is a multimission laboratory managed and operated by Na-

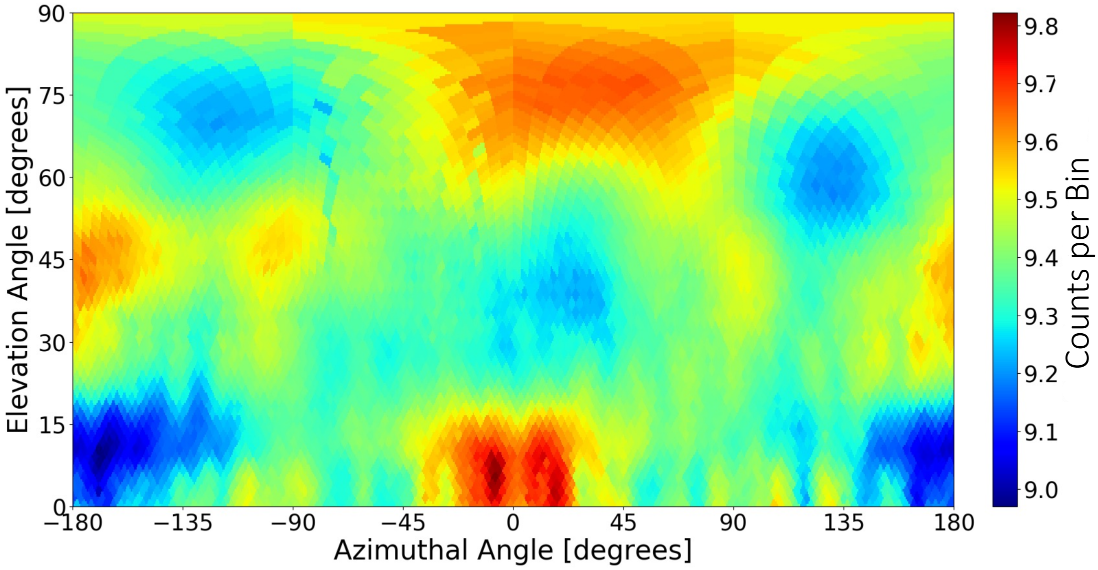

(a)

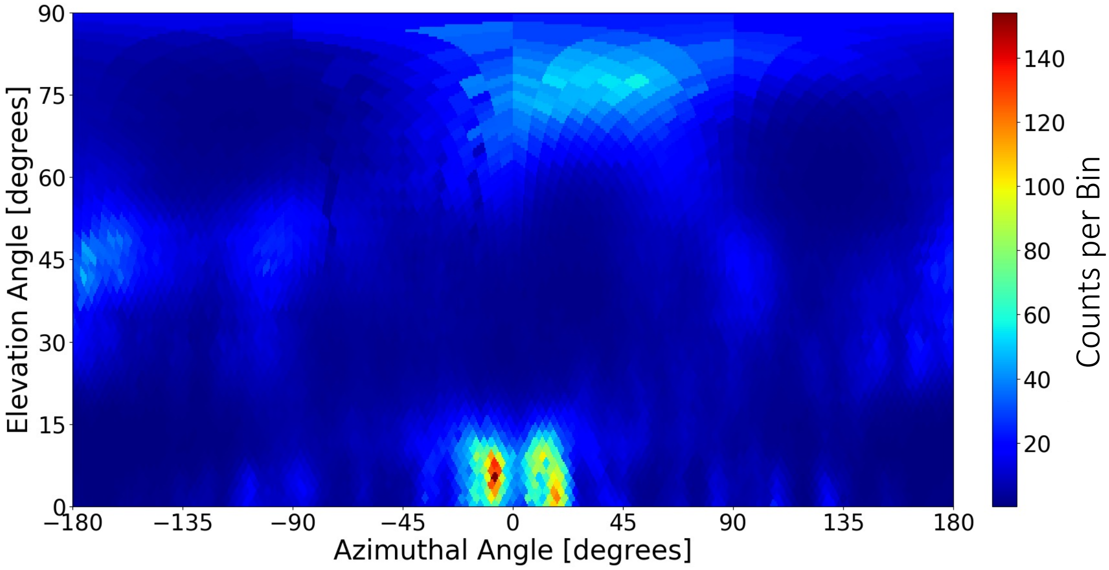

(b)

Figure 13: (a) First MLEM source location estimation of 5.03×10^4 observed background neutrons shows a preferential neutron source location at low elevations corresponding to the vault where two shielded neutron sources are stored. (b) 99th MLEM source location estimation of background neutrons converges towards the location of the two shielded sources stored inside the vault.

tional Technology & Engineering Solutions of Sandia, LLC, a wholly owned subsidiary of Honeywell International Inc., for the U.S. Department of Energy's National Nuclear Security Administration under contract DE-NA0003525. The views and conclusions contained in this document are those of the authors and should not be interpreted as necessarily representing the official policies, either expressed or implied, of the U.S. Department of Homeland Security. The authors thank the US DOE National Nuclear Security Administration, Office of Defense Nuclear Nonproliferation Research and Development for funding a portion of this work. This research used the Savio computational cluster resource provided by the Berkeley Research Computing program at the University of California, Berkeley (supported by the UC Berkeley Chancellor, Vice Chancellor for Research, and Chief Information Officer).

References

[1] S. Croft, A. Favalli, Review and evaluation of the spontaneous fission half-lives of 238pu, 240pu, and 242pu and the corresponding specific fission rates, Nuclear Data Sheets 175 (2021) 269–287. doi:https://doi.org/10.1016/j.nds.2021.06.003.

[2] M. F. L'Annunziata, 1 - nuclear radiation, its interaction with matter and radioisotope decay, in: M. F. L'Annunziata (Ed.), Handbook of Radioactivity Analysis (Second Edition), second edition Edition, Academic Press, San Diego, 2003, pp. 1–121. doi:https://doi.org/10.1016/B978-012436603-9/50006-5.

[3] M. Chadwick, P. Oblozinsky, M. Herman, N. Greene, R. Mcknight, D. Smith, P. Young, R. Macfarlane, G. Hale, S. Frankle, A. Kahler, T. Kawano, R. Little, D. Madland, P. Moller, R. Mosteller, P. Page, P. Talou, H. Trellue, M. White, W. Wilson, R. Arcilla, C. Dunford, S. Mughabghab, B. Pritychenko, D. Rochman, A. Sonzogni, C. Lubitz, T. Trumbull, J. Weinman, D. Brown, D. Cullen, D. Heinrichs, D. Mcnabb, H. Derrien, M. Dunn, N. Larson, L. Leal, A. Carlson, R. Block, J. Briggs, E. Cheng, H. Huria, M. Zerkle, K. Kozier, A. Courcelle, V. Pronyaev, S. Marck, Endf/b vii.0: Next generation evaluated nuclear data library for nuclear science and technology (107) (2006-01-01 2006).

[4] R. C. Runkle, A. Bernstein, P. E. Vanier, Securing special nuclear material: Recent advances in neutron detection and their role in nonproliferation., Journal of Applied Physics 108 (11) (2010) 111101–01–111101–21.

[5] Passive Nondestructive Assay of Nuclear Materials., Los Alamos National Laboratory, 2013.

[6] M. S. Gordon, P. Goldhagen, K. P. Rodbell, T. H. Zabel, H. H. K. Tang, J. M. Clem, P. Bailey, Measurement of the flux and energy spectrum of cosmic-ray induced neutrons on the ground, IEEE Transactions on Nuclear Science 51 (6) (2004) 3427–3434.

[7] J. Lopez, K. Terao, J. Conrad, D. Dujmic, L. Winslow, A prototype detector for directional measurement of the cosmogenic neutron flux, Nuclear Instruments and Methods in Physics Research Section A: Accelerators, Spectrometers, Detectors and Associated Equipment 673 (2012) 22–31. doi:https://doi.org/10.1016/j.nima.2012.01.021.

[8] A. Iyengar, M. Beach, R. Newby, L. Fabris, L. Heilbronn, J. Hayward, Systematic measurement of fast neutron background fluctuations in an urban area using a mobile detection system, Nuclear Instruments and Methods in Physics Research Section A: Accelerators, Spectrometers, Detectors and Associated Equipment 773 (2015) 27–32. doi:https://doi.org/10.1016/j.nima.2014.10.045.
URL `https://www.sciencedirect.com/science/article/pii/S0168900214012029`

[9] J. R. Davis, E. Brubaker, K. Vetter, Fast neutron background characterization with the radiological multi-sensor analysis platform (radmap), Nuclear Instruments and Methods in Physics Research Section A: Accelerators, Spectrometers, Detectors and Associated Equipment 858 (2017) 106 – 112. doi:https://doi.org/10.1016/j.nima.2017.03.042.

[10] A. Glick, E. Brubaker, B. Cabrera-Palmer, M. Gerling, B. J. Quiter, K. Vetter, Deployment of a double scatter system for directional detection of background neutron radiation, Nuclear Instruments and Methods in Physics Research Section A: Accelerators, Spectrometers, Detectors and Associated Equipment (2021) 165029doi:https://doi.org/10.1016/j.nima.2021.165029.
URL http://www.sciencedirect.com/science/article/pii/S0168900221000139

[11] K. Murakami, H. Yoshida, A geant4-python interface : Development and its applications, in: 2006 IEEE Nuclear Science Symposium Conference Record, Vol. 1, 2006, pp. 98–100.

[12] Openscad: the programmers solid 3d cad modeller (Jun 2017).
URL http://www.openscad.org/

[13] M. Monterial, P. Marleau, S. Clarke, S. Pozzi, Application of bayes' theorem for pulse shape discrimination, Nuclear Instruments and Methods in Physics Research A 795 (2015) 318–324.

[14] T. C. S. Rendall, C. B. Allen, Efficient mesh motion using radial basis functions with data reduction algorithms, Journal of Computational Physics 228 (2009) 6231–6249.

[15] Healpix: Data analysis, simulations and visualization on the sphere, https://healpix.sourceforge.io/, accessed: 2020-04-01.

[16] L. A. Shepp, Y. Vardi, Maximum likelihood reconstruction for emission tomography, IEEE Transaction on Medical Imaging 1 (1982) 113 – 122.

[17] N. Bissantz, B. Mair, A. Munk, A multi-scale stopping criterion for mlem reconstructions in pet, 2006, pp. 3376 – 3379. doi:10.1109/NSSMIC.2006.353726.

[18] L. Montgomery, A. Landry, G. Al Makdessi, F. Mathew, J. Kildea, A novel mlem stopping criterion for unfolding neutron fluence spectra in radiation therapy, Nuclear Instruments and Methods in Physics Research Section A: Accelerators, Spectrometers, Detectors and Associated Equipment 957 (2020) 163400. doi:https://doi.org/10.1016/j.nima.2020.163400.
URL https://www.sciencedirect.com/science/article/pii/S0168900220300061